Exchange bias effect in Au-Fe_{3}O_{4} dumbbell nanoparticles induced by the charge transfer from gold

Mikhail Feygenson, John C. Bauer, Zheng Gai, Carlos Marques, Meigan C. Aronson, Xiaowei Teng, Dong Su, Vesna Stanic, Volker S. Urban, Kevin A. Beyer, and Sheng Dai

Phys. Rev. B **92**, 054416 — Published 10 August 2015

DOI: 10.1103/PhysRevB.92.054416

Exchange bias effect in Au-Fe_3O_4 dumbbell nanoparticles induced by the charge transfer from gold

Mikhail Feygenson,[1] John C. Bauer,[2] Zheng Gai,[3] Carlos Marques,[4] Meigan C. Aronson,[4,5] Xiaowei Teng,[6] Dong Su,[7] Vesna Stanic,[8] Volker S. Urban,[9] Kevin A. Beyer,[10] and Sheng Dai[2]

[1]*Chemical and Engineering Materials Division, Spallation Neutron Source, Oak Ridge National Laboratory, Oak Ridge, Tennessee 37831, USA**

[2]*Chemical Sciences Division, Oak Ridge National Laboratory, Oak Ridge, Tennessee 37831, USA*

[3]*Center for Nanophase Materials Sciences, Oak Ridge National Laboratory, Oak Ridge, TN 37831, USA*

[4]*Department of Physics and Astronomy, Stony Brook University, Stony Brook NY 11794, USA*

[5]*Condensed Matter Physics and Materials Science Department, Brookhaven National Laboratory, Upton, New York 11973-5000, USA*

[6]*Department of Chemical Engineering, University of New Hampshire, Durham, NH 03824, USA*

[7]*Center for Functional Nanomaterials, Brookhaven National Laboratory, Upton, NY 11973, USA*

[8]*Photon Sciences Directorate, Brookhaven National Laboratory, Upton, New York, 11973, USA*

[9]*Biology and Soft Matter Division, Oak Ridge National Laboratory, Oak Ridge, Tennessee 37831-6475, USA*

[10]*X-ray Science Division, Argonne National Laboratory, Argonne, IL 60439, USA*

Abstract

We have studied the origin of the exchange bias effect in the Au-Fe_3O_4 dumbbell nanoparticles in two samples with different sizes of the Au seed nanoparticles (4.1 and 2.7 nm) and same size of Fe_3O_4 nanoparticles (9.8 nm). The magnetization, small-angle neutron scattering, synchrotron x-ray diffraction and scanning transmission electron microscope measurements determined the antiferromagnetic FeO wüstite phase within Fe_3O_4 nanoparticles, originating at the interface with the Au nanoparticles. The interface between antiferromagnetic FeO and ferrimagnetic Fe_3O_4 is giving rise to the exchange bias effect. The strength of the exchange bias fields depends on the interfacial area and lattice mismatch between both phases. We propose that the charge transfer from the Au nanoparticles is responsible for a partial reduction of the Fe_3O_4 into FeO phase at the interface with Au nanoparticles. The Au-O bonds are formed, presumably across the interface to accommodate an excess of oxygen released during the reduction of magnetite.

I. INTRODUCTION

In recent years, Au-Fe_3O_4 dumbbell nanoparticles have been widely studied because of their applications in magnetic resonance imaging[1–3], hyperthermia treatment[4], drug delivery[5], DNA-based biosensors[6] and catalysis[7,8]. The most intriguing property of Au-Fe_3O_4 dumbbell nanoparticles is the exchange bias (EB) effect reported by several groups[9–11]. When a ferromagnet is in close proximity to an antiferromagnet, the direct exchange interaction between the moments in each can create an unidirectional anisotropy which impedes the reversal of the ferromagnetic moment. The magnetization loop is subsequently shifted along the field axis by the exchange bias field (H_{EB}). The EB effect is well understood in thin films, but it is a more complex phenomenon in magnetic nanoparticles. Size of nanoparticles, their crystallinity and oxidation state can greatly affect the strength of H_{EB} in nanoparticles. Previous experiments on Co-core/CoO-shell nanoparticles found that H_{EB} depends on a net magnetic moment at core-shell interface induced by lattice strain between Co core and CoO shell[12]. The variation of this moment with the strain is ultimately responsible for nonmonotonically dependence of H_{EB} on Co core thickness, in contrast to Co/CoO thin films, where the same dependence is inversely linear. A core/shell interface is not the only prerequisite for the EB in magnetic nanoparticles. For example, in single component NiO nanoparticles presence of uncompensated magnetic sublattices led to the horizontal shift of the magnetization loop, reminiscent of the EB[13]. Considering that the magnetic and structural properties of Fe_3O_4 and Au nanoparticles are greatly modified from their bulk counterparts[14–17] there are several possible explanations of the origin of the EB effect in the dumbbell nanoparticles. The bulk Fe_3O_4 is a ferrimagnetic (FiM) material with inverse spinel structure and lattice constant which is almost double (8.396 Å) of that of gold (4.083 Å). The bulk gold is weakly diamagnetic, however 1.5 nm Au nanoparticles can sustain localized magnetic moments and show a ferromagnetic-like behavior when capped with the thiol-ligand shell, due to 5d localized holes generated by the charge transfer from Au to S[18]. Thus, ferromagnetic/ferrimagnetic coupling between Au and Fe_3O_4 nanoparticles can lead to the EB, similar to Fe-core/γ-Fe_2O_3-shell nanoparticles[19]. The magnetic structure of 9 nm Fe_3O_4 nanoparticles was found to be nonuniform and consists of magnetically ordered core and surface shell of canted spins[15]. The number of those canted spins is presumably increased at the Au/Fe_3O_4 interface in the dumbbell nanoparticles[9]. The coupling between

the ordered core and canted shell can lead to the EB, as well, and it was observed for single component $NiFe_2O_4$ and γ-Fe_2O_3 nanoparticles[19,20]. Similar explanation is based on the exchange coupling between antiphase boundaries (APBs) with canted spins and FiM regions within Fe_3O_4 nanoparticles. The APBs were experimentally observed in magnetite thin films grown on MgO substrate, which has a cubic structure similar to Au[21,22]. Finally, the exchange bias might arise from exchange interactions between ferrimagnetic Fe_3O_4 and antiferromagnetic FeO phases. The FeO phase can originate at Au/Fe_3O_4 interface due to the charge transfer from gold which reduces Fe_3O_4 into FeO. This explanation was first suggested by Pineider *et al*,[23] to explain the exchange bias effect in Au/Iron oxide core-shell nanoparticles.

The EB effect in the Au-Fe_3O_4 dumbbell nanoparticles depends on sample preparation and measurements details. When the reaction solvent is slightly polarized multiple nucleation sites on the surface of Au seed nanoparticles become available for Fe_3O_4, resulting in flower-like structures[11]. The flower-like structures show significantly larger exchange bias fields as compared to dumbbells[10]. In the powder form, the blocking temperature of the Au-Fe_3O_4 dumbbell nanoparticles is increased due to inter-particle interactions[11,24]. Moreover, close-packing of nanoparticles can lead to the EB effect due to partial restoration of the bulk-like magnetic properties, reported in Co/CoO nanoparticles[25].

In order to understand the origin of the EB effect in such complex system like Au-Fe_3O_4 dumbbell nanoparticles, it is crucial to obtain the experimental data on particle dimensions, crystallinity and possible inter-particle interactions. Because we are interested in the length scales ranging from interatomic distances of a few Angstroms, to extended structures of tens of nanometers, several experimental techniques have to be combined. Experimental studies of a crystal structure of nanoparticles have always been a challenge. Conventional Rietveld refinements of the powder diffraction data often fail to provide an adequate picture of the crystal structure of nanoparticles. Small size, defects and lack of translational symmetry in nanoparticles result in broad and overlapping Bragg peaks. Often, crucial information about local crystal structure is hindered in diffuse scattering, which is orders of magnitude lower than Bragg peak intensities and ignored during Rietveld analysis. The pair-distribution function (PDF) analysis of diffraction data has been successfully applied to address this challenge. In PDF analysis both diffuse and Bragg scattering are analyzed simultaneously, thus providing insights into crystal structure and disorder in nanoparticles.

TABLE I: Size and size distribution of the dumbbell samples obtained by TEM, SANS and SAXS measurements. H_{EB} is the exchange bias field at 2 K.

sample	Au-4		Au-3	
	Fe_3O_4	Au	Fe_3O_4	Au
R_{TEM}(nm)	7.8±1.2	4.1±1.7	7.8±1.4	2.7±0.6
R_{SANS}(nm)	-	-	8.5±1.5	2.3±0.3
R_{SAXS}(nm)	9.3±1.2	3.8±0.4	9.8±1.2	2.8±0.7
H_{EB}(Oe)	1919(6)		1350(7)	

In this work we present a study of two Au-Fe_3O_4 dumbbell nanoparticles with the same sizes (R=9.8 nm) of Fe_3O_4 nanoparticles, but different sizes of Au seed nanoparticles. These are 4.1 and 2.7 nm for the samples Au-4 and Au-3, respectively (see Tab. I). We will use a combination of magnetization, transmission microscopy, small-angle neutron and x-ray scattering measurements to accurately determine the Au and Fe_3O_4 nanoparticle dimensions, and demonstrate that inter-particle interactions play no appreciable role in the exchange bias effect. Magnetization and synchrotron x-ray diffraction measurements confirm that the antiferromagnetic FeO phase forms within Fe_3O_4 nanoparticle, presumably at the Au/Fe_3O_4 interface. The exchange bias occurs as a result of the coupling between antiferromagnetic FeO and ferrimagnetic Fe_3O_4 phases. By appealing to x-ray absorption spectroscopy experiments carried out on similar samples[27,28], and to PDF analysis of diffraction data, we argue that FeO phase is induced by the charge transfer from Au nanoparticles. The relation between H_{EB} and crystal structure of Au and Fe_3O_4 nanoparticles is also discussed.

II. SAMPLES AND EXPERIMENTS

Monodisperse Au seed nanoparticles were first synthesized using a procedure developed by Sun *et al*,[29,30]. $HAuCl_4 \cdot 3H_2O$ (200 mg, 0.5 mmol) was dissolved in a solution of tetralin (20 mL) and oleylamine (20 mL) by stirring under N_2 atmosphere at 0^o C or 20^oC to obtain a particle size near R = 4 and 3 nm, respectively. Then a reducing solution, made by dissolving tert-butylamine-borane complex (88 mg, 1.0 mmol) in 2 mL of tetralin and 2 mL of oleylamine by sonication, was rapidly injected into the Au solution. The solution changed

from an orange color to brown and then gradually into red. The product was diluted in ethanol and collected by centrifuging at 8000 rpm for 10 min.

To synthesize Au-Fe_3O_4 dumbbell nanoparticles a procedure described in[31] was used and is briefly outlined. The reaction began by stirring a solution of 1 ml oleic acid (3 mmol) in 20 ml 1-octadecene under a flow of N_2 at 120^{o}C for 20 min. Then 0.3 mL of $Fe(CO)_5$ (2 mmol) was injected into the solution under N_2 atmosphere and stirred for 5 minutes. 0.5 ml of oleylamine was injected into the mixture, followed by an appropriate volume of the Au nanoparticle solution to equal approximately 20 mg. The solution was heated to reflux ($\sim$310^{o}C) for 45 minutes. After the reaction cooled down to room temperature the solution was diluted in ethanol and centrifuged at 7500 rpms for 10 minutes and redispersed into hexane or d-toluene prior to magnetization and scattering measurements.

The DC magnetization measurements were carried out using a Quantum Design Magnetic Property Measurement System (MPMS). For the measurements, 10 μL of the original aliquots were dispersed in 50 μL of liquid paraffin and then injected into a standard gelatin capsule to reduce inter-particle interactions. The gelatin capsules were fastened in plastic straws for immersion into the magnetometer. In order to measure the exchange bias field, a sample is cooled from 300 K to a target temperature in an applied magnetic field of 50 kOe. The magnetization is then measured as a function of an applied magnetic field. The exchange bias field is calculated as $H_{EB} = |H_{c1} - H_{c2}|/2$, where H_{c1} and H_{c2} are the negative and positive coercive fields, respectively. The standard field-cooled (FC) and zero-field cooled (ZFC) measurements of temperature-dependent magnetization were used to define the blocking temperature (T_B). FC and ZFC measurements were carried out in the field of 500 Oe.

The small-angle neutron scattering (SANS) experiments were conducted with the Bio-SANS (CG-3) instrument at the High Flux Isotope Reactor in the Oak Ridge National Laboratory with a neutron wavelength of 6.09 Å[32]. The samples were dispersed in deuterated toluene to reduce incoherent scattering from hydrogen. Sample to detector distances of 0.3 and 14 m were used to cover the q-range from 0.003 to 0.67 Å^{-1}, where q is the scattering vector defined as $q = 4\pi/\lambda \sin\theta$, with λ and θ are the neutron wavelength and scattering angle, respectively. The data was corrected for the detector sensitivity, sample transmission and background scattering from d-toluene.

The synchrotron small-angle x-ray scattering (SAXS) measurements were carried out at the

beamline X6B at the National Synchrotron Light Source at Brookhaven National Laboratory using x-rays with wavelength λ=1.24 Å. The X6B beamline was configured for SAXS experiment with sample to detector distance of 120 mm. The magnetic field of 1.2 Tesla was applied perpendicular to the incoming beam. The samples were in the original solution. The data was corrected for the beam attenuation, dark current and the background scattering from solution. The SANS and SAXS data were analyzed using software from the NIST Center for Neutron Research[33].

The synchrotron x-ray pair distribution function (PDF) measurements were carried out at the beamlines 11-ID-B (λ=0.2127 Å) and 6-ID-C (λ = 0.12488 Å) at the Advanced Photon Source, Argonne National Laboratory. The dried powders were measured in a 0.5 mm kapton capillary. The standard Ni bulk was measured to estimate the resolution of each instrument. The measurements were carried out at room temperature in ambient conditions. The sample Au-3 was measured at 11-ID-B with a short detector-to-sample distance (D) of 110 mm. We had only 4 mg of the sample available, thus using shorter D allowed to gain more intensity. In contrast, we used the high q-resolution configuration (D=240.5 mm) to measure Au-4 sample at 6-ID-C. The bulk Au and mixture of Fe_3O_4 and α-Fe_2O_3 bulk powders were measured under the same experiential conditions as a reference. The PDF data were analyzed using the PDFgui program[34].

III. RESULTS

Transmission electron microscopy (TEM) measurements of the as-synthesized Au-4 sample (Fig.1(a)) show a large population of dumbbell nanoparticles, with darker contrast indicating Au and lighter one Fe_3O_4 nanoparticles. Both particles appear to be nearly spherical and fairly monodisperse. Analysis of TEM images reveals the average radius of 4.1±1.7 and 7.8±1.2 nm for Au and Fe_3O_4 nanoparticles, respectively (Fig.1(b)). The electron diffraction rings of a single dumbbell nanoparticle (Fig.1(c)) are well indexed with two phases: face-centered cubic (fcc) Au and inverse spinel structure of Fe_3O_4. We find that free Fe_3O_4 nanoparticles are present in the sample, because some Fe atoms did not precipitate onto Au nanoparticles and self-reduced into free iron nanoparticles, which were later oxidized into magnetite. Some of the particles appear to have a 'flower'-like morphology, presumably due to coalescence of individual magnetite nanoparticles. Such variations in particle's shape are

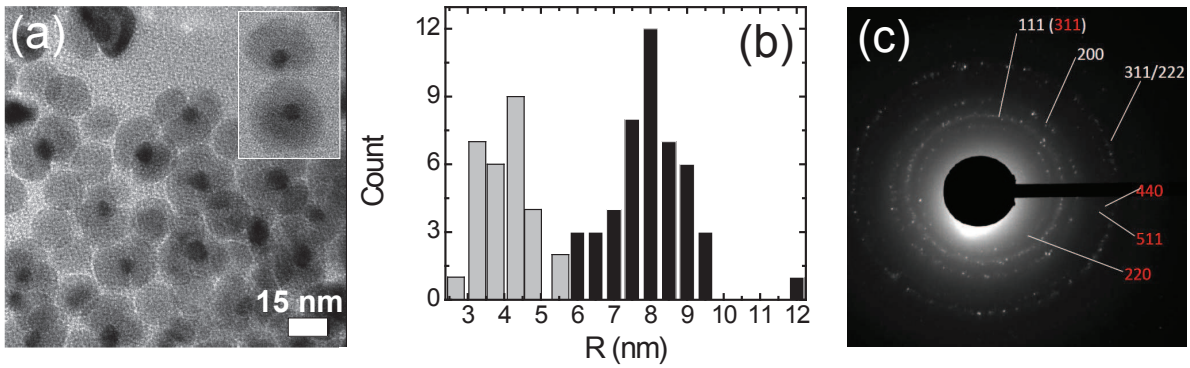

FIG. 1: (a) A representative TEM image of the sample Au-4. The darker contrast indicates Au nanoparticles and the lighter one indicates Fe_3O_4 nanoparticles. Inset confirms a dumbbell shape of nanoparticles. (b) The size distribution of Fe_3O_4 (black bars) and Au (grey bars) nanoparticles, obtained from analysis of several TEM images. (c) The electron diffraction pattern of a single nanoparticle in the sample Au-4. The red numbers indicate to Fe_3O_4 spinel structure reflections, white numbers are reflections corresponding to the Au face-centered cubic structure.

undesirable, because it complicates the modeling of small-angle and PDF data. Moreover, agglomeration of magnetic nanoparticles leads to formation of a disordered interface which can induce the exchange bias. The centrifugation of nanoparticles and their dispersion in paraffin were employed to reduce the shape effects on the scattering data modeling and exchange bias, respectively.

We compare magnetic properties of the sample Au-4 with the reference sample, consisting of the mixture of single component Au and Fe_3O_4 nanoparticles with the similar sizes (Fig.2). The ZFC magnetization of the dumbbell nanoparticles is steadily increasing from 2 K up to 190 K, where the sharp upturn is observed. The upturn corresponds to antiferromagnetic (AFM) phase transition at the Néel temperature T_N=190 K of FeO, previously reported in FeO/Fe_3O_4 core-shell nanoparticles[35,36,39]. These results provide limited evidence that the FeO phase is antiferromagnetically ordered below 190 K, although temperature-dependent neutron diffraction measurements are required to unambiguously determine its magnetic state. Above $T_B \sim 200$ K ZFC magnetization is merged with the FC magnetization. The blocking temperature of magnetic nanoparticles is related to the energy barrier $\triangle$E separating two preferred directions of magnetization via Arrhenius's law $T_B \approx \triangle E/k_b$, where k_b is the Boltzmann constant[40]. If dipolar inter-particle interactions are present $\triangle E = KV + E_{int}$,

where K is the magnetocrystalline anisotropy constant, V is the particle magnetic volume and E_{int} is the energy of interactions[41,42]. In our previous work, we demonstrated that dilution in paraffin weakens the dipolar interactions of Co/CoO nanoparticles to the extent that no measurable effect on the blocking temperature was detected[12]. Thus, we conclude that increase of T_B in the dumbbell nanoparticles is due to the exchange biasing, as previously reported for the magnetic core-shell nanoparticles[12,23,35,36]. Mixture of Fe_3O_4 and Au nanoparticles show two blocking temperatures T_{B1}=25 K and T_{B2}=283 K (Fig.2b), with no indications of the AFM transition at 190 K. Using K=$1.35 \cdot 10^5$ erg/cm^3 for the bulk magnetite[14] and assuming no interactions, we estimated the radius of the magnetite nanoparticles to be 5.5 and 12.2 nm, respectively. Our estimations are approximate, since the enhancement of the effective magnetic anisotropy from its bulk value was observed in iron oxide nanoparticles[14,37,38]. The latter is smaller than the radius of Fe_3O_4 nanoparticles obtained with TEM, because magnetic volume is reduced due to the shell of canted spins[15,43,44]. The former corresponds to the larger agglomerates of Fe_3O_4 nanoparticles, occasionally observed with TEM in the free magnetite nanoparticles sample. It is worth noting that ZFC M(T) changes the slope at $\sim$ 100 K in both dumbbell (Fig.2a and Fig.7a) samples and reference (Fig.2b) sample. We attribute this change to the Verwey transition, which is observed at substantially reduced temperature relative to that of bulk magnetite, which is 120 K[45]. The reduction of Verwey temperature and broadening of ZFC magnetization around transition are consistent with the previous magnetization measurements of magnetite nanoparticles[14,46,47].

In order to further investigate the origin of T_B enhancement in the dumbbell nanoparticles we carried out field-dependent magnetization loop measurements. Fig.2(c) shows the magnetization loop M(H) of the sample Au-4, after cooling from room temperature in a field of 50 kOe to various target temperatures. The dumbbell nanoparticles show a substantial shift of the loop towards negative fields. The loop shift is due to the exchange bias, which is likely due to exchange coupling of ferrimagnetic Fe_3O_4 with antiferromagnetic FeO phase, evident in M(T) measurements. The maximum exchange bias field of 1919 Oe at 2 K was observed for the sample Au-4, while it is significantly lower (1350 Oe) in the sample Au-3. We see that H_{EB} first becomes nonzero at $T_B \sim$200 K in each dumbbell sample and increases with decreasing temperature (Fig.3). In contrast, H_{EB} remains zero at all temperatures for solution of single component Au and Fe_3O_4 nanoparticles under the same experimental conditions.

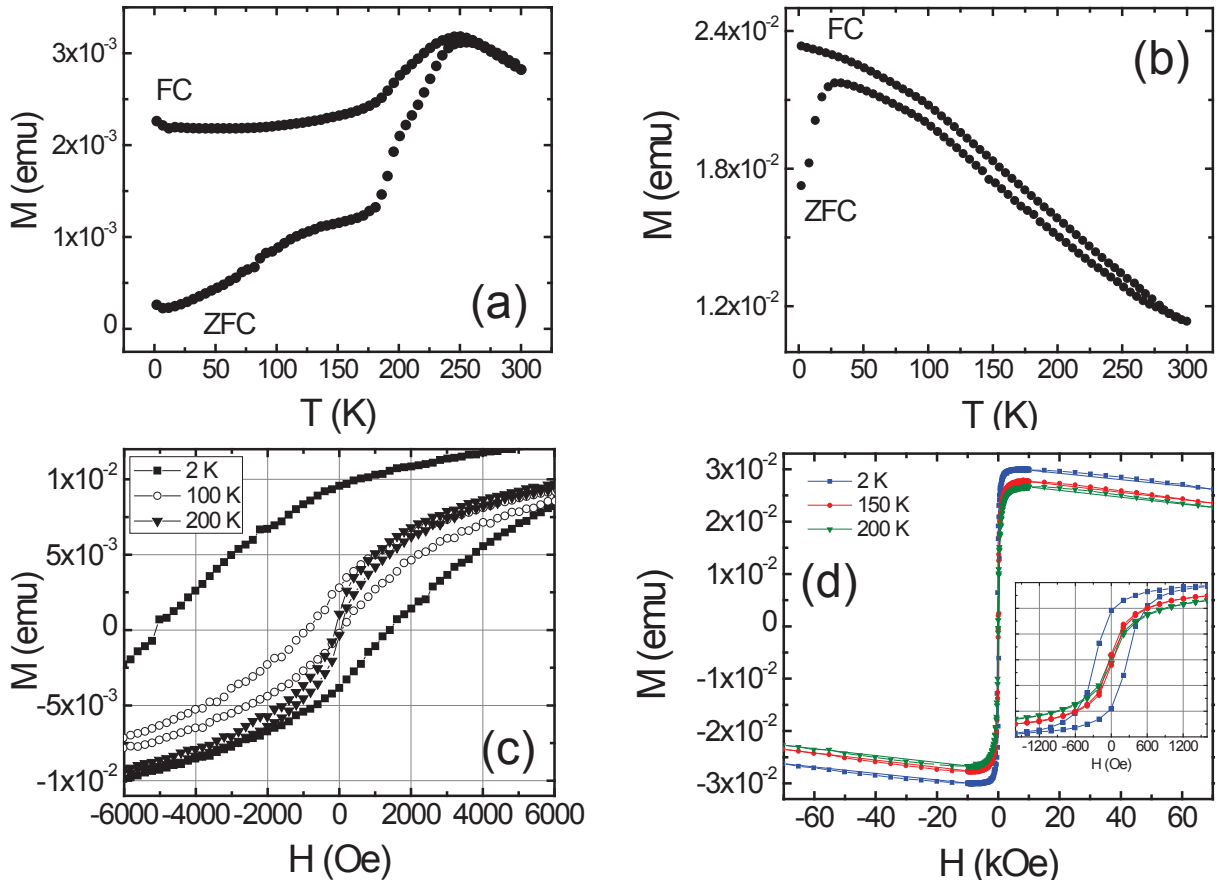

FIG. 2: Temperature-dependent ZFC and FC magnetizations for (a) Au-4 sample and (b) free solution of Fe_3O_4 and Au nanoparticles. The field-dependent magnetization measured after field cooling in 50 kOe from 300 K for (c) Au-4 and (d) reference samples at various temperatures. Inset: the same plot at lower fields, showing no horizontal shift of the hysteresis loop.

The absence of the loop shift is in agreement with M(T) measurements, which showed no indication of the FeO phase. We note that in our dumbbell nanoparticles the T_B appears to be slightly higher than T_N. Despite the exchange bias effect was reported for the samples with $T_B > T_N$[48], neutron diffraction measurements are required for determining the T_N of our nanoparticles[49].

Combination of SANS and SAXS experiments are used to provide independent measurements of the dumbbell nanoparticles dimensions, and to probe possible inter-particle interactions. Neutrons are sensitive to the light elements, hence ligand coated dumbbell nanoparticles provide a sharp core-shell contrast for neutrons (inset in Fig.4a). X-rays are more sensitive to heavy elements and simpler core contrast for the dumbbell nanoparticles

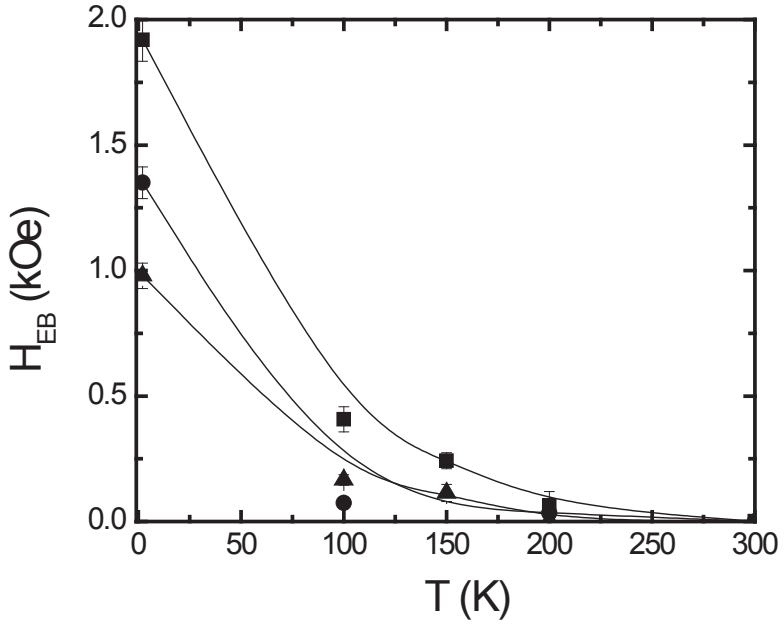

FIG. 3: The exchange bias field H_{EB} as a function of temperature for (■) Au-4, (●) Au-3 and (▲) aged Au-3 sample. Solid lines are guides for the eye.

is realized (inset in Fig.4c). Our TEM studies indicated that the dumbbell sample consists of epitaxially linked polydisperse Au and Fe_3O_4 nanoparticles coated with OA/olyemine ligands. To the best of our knowledge, no scattering form-factor describing such system has been reported. Thus, we first studied as-synthesized dumbbell sample Au-3 after refluxing. At this stage, the sample contains a dispersion of seed Au nanoparticles and slowly nucleating Fe_3O_4 nanoparticles. Analysis of this sample will provide us with dimensions of Au nanoparticles in the dumbbell sample. We then fix them during refinement of the dumbbell sample, which will make it more reliable. The nucleation has completed after 12 hours, significantly slower that the averaged SANS measurement time of 2 hours. SANS intensity for the as-synthesized Au-3 sample is plotted as a function of the scattering vector q in Fig.4a. The q-dependence of the SANS intensity is fitted using a sum of two form factors. The first form factor describes spherical Au-core/OA-shell nanoparticles assuming a polydispersed core and monodispersed shell. The second form factor is the same, with Fe_3O_4-core/OA-shell structure. During the fitting we fix the scattering length densities of the Au, Fe_3O_4, OA and d-toluene to their bulk values in order to reduce the number of free parameters. The best fit is represented by the solid line in Fig.4a. SANS measurements

indicate a presence of spherical Au nanoparticles with R=2±1 nm and small clusters of Fe_3O_4 with R=1±0.3nm. Size of Au nanoparticles is in excellent agreement with the TEM results. Dashed line in Fig.4a is the fit with the form factor of Au nanoparticles only, which poorly reproduces the data at low q. The implication is that both form factors for spherical nanoparticles of Au and Fe_3O_4 are required to obtain the best fit to our data. Figure 4b shows SANS intensity of the Au-3 sample, after nucleation of Fe_3O_4 nanoparticles has been completed. Again, we used a sum of two models to describe scattering pattern from the dumbbell nanoparticles. Each model is a form factor for core-shell nanoparticles[50] multiplied by the structure factor described by Teixeira[51] for the fractal-like aggregates. The form and structure factor are calculated for Au and Fe_3O_4 nanoparticles and SANS intensity is then fitted to the sum of both models. Inclusion of the structure factor added two more free parameters, fractal dimension D and correlation length L. In order to reduce number of free parameters and obtain a stable fit we fixed the size of Au nanoparticles and ligand-shell thickness to the values obtained from the refinements of SANS data for the as-synthesized Au-3 sample (Tab.II). The scattering length densities of Au, Fe_3O_4, OA and d-toluene were also fixed. The best fit is depicted as a solid line in Fig.4b. The radius of Fe_3O_4 nanoparticles derived from the fit is R=8.5±1.5nm. We note that our model fails to reproduce the experimental data at q>0.7 $Å^{-1}$, because it ignores an average of the dumbbells over all possible orientations[52,53]. Moreover, the polydispersity of nanoparticles derived from refinements are likely overestimated, because smearing effects of the finite q-resolution were not taken into account. Development of a more realistic two-phase model with polydisperse core-shell building blocks is currently underway. The quality of the SANS fit is ambiguous at higher q, and thus we repeated the small-angle measurements using synchrotron x-rays (Fig.4c) for both dumbbell samples. The dumbbell nanoparticles provide the core-contrast for x-rays (see inset Fig.4c), therefore we used a simplified two-fractals model, for polydisperse core particles without a shell[51]. The SAXS measurement of the sample Au-3 finds that the size of Au (R=2.7±0.7nm) nanoparticles consistent with SANS and TEM results. The size of Fe_3O_4 nanoparticles is found to be 9.8±1.2 and 9.3±1.2 nm for the sample Au-3 and Au-4, respectively (Tab.III). The values are somewhat higher than the values obtained by TEM measurements. Magnetite has a brighter contrast in TEM and presence of the overlapping particles makes it difficult to reliable extract dimensions of Fe_3O_4 nanoparticles on a limited sample area.

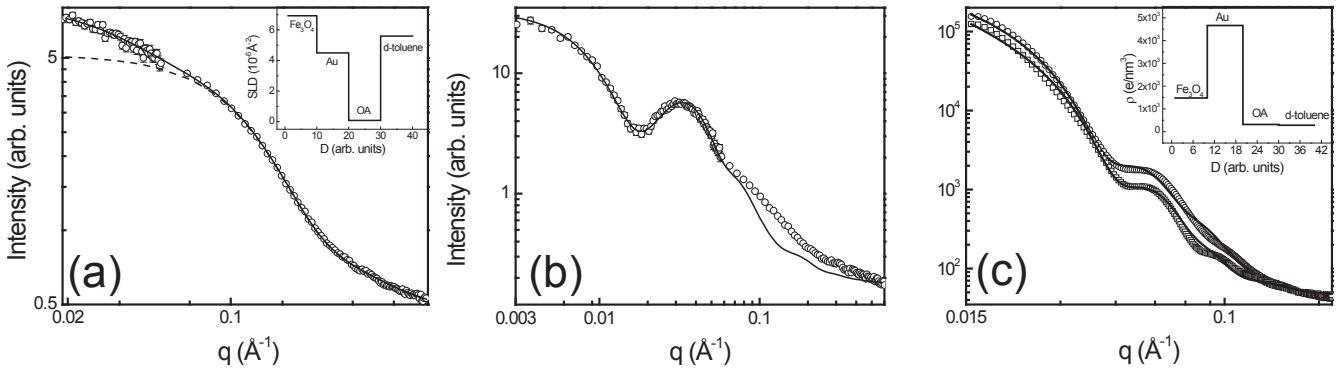

FIG. 4: (a) SANS data at 300 K (open circles) for the as-synthesized Au-3 sample. Solid line is the fit to the model of spheres with bimodal Schulz size distribution. Dotted line is the model with the polydisperse Au nanoparticles only. (b) SANS data for the same sample after 12 hours. Solid line is the best fit with two fractal models. (c) SAXS data for both Au-3 (◯) and Au-4 (□) samples. Solid lines are the fits to the model of two fractals with polydisperse spheres. Insets in (a) and (c) are the the scattering length density (SLD) and electron density (ϱ) profiles, respectively.

If magnetic interactions between nanoparticles are significant the scattering intensity would depend on the magnitude of an applied magnetic field[54–57]. We subject the solution of the dumbbell nanoparticles into the magnetic field and found no considerable difference between SAXS intensities measured at 0 and 1.2 T for both samples. Therefore, the inter-particle interactions play no role in the magnetic processes, including enhancement of T_B in the dumbbell nanoparticles. SANS results indicate that Au nanoparticles are coated with the surfactant in the dumbbell nanoparticles. It is unlikely, however that the ferromagnetism was induced in Au nanoparticles by the ligands. The ZFC M(H) measurements of the mixture of Au and Fe_3O_4 nanoparticles, showed the ferrimagnetic-like response with the coercivity field and saturation magnetization both consistent with the values reported for the bulk Fe_3O_4[21]. We tried to improve SANS and SAXS fits by introducing the FeO phase, which is evident from magnetization measurements, by adjusting the scattering cross-section of the Fe_3O_4 nanoparticles. For x-rays the difference between FeO and Fe_3O_4 phases in electron density is about 10% (1637 and 1478 e/nm^3, respectively). The contrast is even weaker for neutrons, with difference in SLD less than 6% ($7.3{\cdot}10^{-6}$ and $6.9{\cdot}10^{-6}$ cm^{-2}). The quality of the SANS and SAXS fits show no improvements, when FeO phase was added. Thus, we carried out synchrotron x-ray diffraction experiments on the dumbbell nanoparticles. Fe_3O_4 has inverse

TABLE II: Results of the SANS refinements of as-synthesized Au-3 sample and the same sample after 12 hours. Where, R_{core} is the radius of the core, σ is the core polydispersity, t_{shell} is the thickness of the shell, D is the fractal dimension, L is the correlation length, SLD_{core}, SLD_{shell} and $SLD_{solv.}$ are the neutron scattering length densities for the core, shell and solvent, respectively.

	Au-3 (fresh)		Au-3	
sample	Au	Fe_3O_4	Au	Fe_3O_4
scale factor	0.02(2)	1.27(1)	0.016(8)	0.115(3)
R_{core}(nm)	2.73(2)	0.61(3)	2.73	8.49(63)
σ	0.46(2)	0.49(2)	0.12(1)	0.17(1)
t_{shell}(nm)	0.29(3)	0.27(2)	0.29	6.13(73)
D			1.0(4)	6.0(5)
L (nm)			0.94(5)	0.47(6)
SLD_{core}(Å^{-2})	4.56e-6	6.84e-6	4.56e-6	6.89e-8
SLD_{shell}(Å^{-2})	8.87e-8	8.87e-8	8.87e-8	8.87e-8
$SLD_{solv.}$(Å^{-2})	5.66e-6	5.66e-6	5.66e-6	5.66e-6
bkg(cm^{-1})	0	0.45	0	0.18

spinel structure, while FeO adopts the cubic structure of NaCl. Both phases should be easily distinguishable with synchrotron x-ray diffraction. Rietveld refinements of the diffraction data for both samples are shown in (Fig.5(a,c)). The best fit was obtained using three cubic phases: Au (space group Fm-3m, Inorganic Crystal Structure Database (ICSD) collection code 52249), magnetite Fe_3O_4 (Fd-3m, ICSD code 27898) and wüstite FeO (Fm-3m, ICSD code 27237). The scale factor, lattice constants and anisotropic displacement parameters (ADPs) were refined for each phase. The constant wavelength x-ray GSAS profile function type 3 was used to describe the peak shapes[58]. The results of the refinements are summarized in Tab.IV. The lattice constant of Au phase in Au-4 sample is close to the reported bulk value of 4.084 Å, while in the sample Au-3, with smaller Au nanoparticles, it is significantly lower (4.051 Å). Conversely, the lattice constant of Fe_3O_4 nanoparticles in Au-3 sample is in the excellent agreement with the bulk value of 8.396 Å, while it is larger for sample Au-4 (8.477 Å). The ADP of oxygen in magnetite is a factor of twenty larger compare to ADP

TABLE III: Summary of the SAXS refinements for Au-3 and Au-4 samples, at room temperature in ambient conditions. R is the block radius, σ is the block polydispersity, D is the fractal dimension, L is the correlation length, SLD and SLD_{solv} is the scattering length density of the block and solvent, respectively.

	Au-3		Au-4	
phase	Au	Fe_3O_4	Au	Fe_3O_4
scale	0.005(1)	0.27(1)	0.003(1)	0.23(1)
R(nm)	2.78(1)	9.87(1)	3.80(2)	9.30(4)
σ	0.25(2)	0.12(1)	0.11(1)	0.12(2)
D	1.6(2)	1.22(1)	3.3(2)	2.2(1)
L(nm)	62.1(2)	233(3)	62.0(3)	288(11)
SLD(Å^{-2})	1.32e-4	4.11(11)e-5	1.32e-4	4.11(9)e-5
SLD_{solv}(Å^{-2})	7.96e-6	7.96e-6	7.96e-6	7.96e-6

of Fe in a and b sites, and has a substantial uncertainty. It is because light elements like oxygen provide a little contrast for x-rays, making reliable refinement of ADP difficult. We attempted to refine the crystallite size broadening parameter to estimate the particle size for each phase. We found this parameter to be highly correlated with the Gaussian terms in the profile function, resulting in unphysically large dimensions of Au nanoparticles. The estimated crystallite size of FeO was 5.3 nm and 3.6 nm for Au-4 and Au-3 samples, respectively. Larger crystallite size of antiferromagnetic FeO can explain higher H_{EB} in Au-4 sample, however we stress that the peak broadening is not directly related to a physical size of nanoparticles. Any relation to a physical size relies on correcting the extracted value with an assumption with regard to the crystallite shape, which is unknown for FeO. Besides, the peak broadening induced by finite crystallite size is rarely Gaussian only[59,60].

Our Rietveld refinements clearly indicate presence of FeO phase, which is not chemically stable and can be spontaneously oxidized into ferrimagnetic Fe_3O_4, antiferromagnetic α-Fe_2O_3(hematite) or ferrimagnetic γ-Fe_2O_3(maghemite) phases[61]. All three phases have distinctive magnetic properties and might contribute to the exchange biasing in the dumbbell nanoparticles. It is challenging to distinguish between maghemite and magnetite phases using a standard Rietveld refinement of a powder x-ray diffraction data due to their sim-

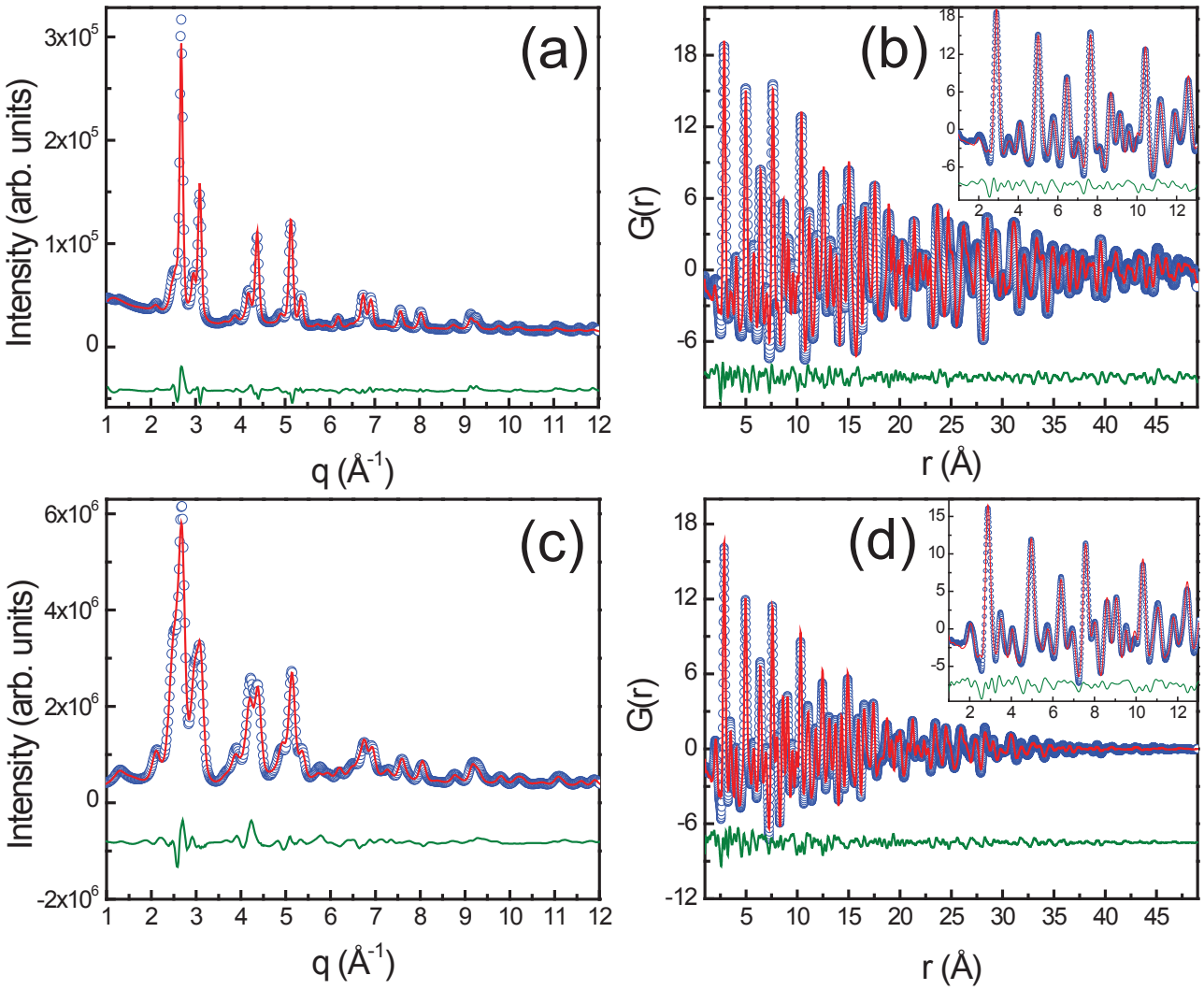

FIG. 5: The Rietveld and PDF analysis for (a,b) sample Au-4 and (c,d) sample Au-3, with experimental data in open circles, calculated pattern in red and difference curve in green. Insets in (b) and (d) are the same data for r=1-13 Å.

ilar crystallinity, however these issues can be overcome by using high-energy synchrotron x-rays[62,63]. The scattering structure factor S(q), with the corrections for background scattering, x-ray transmission and Compton scattering was obtained from the same diffraction data using the PDFgetX2 software package[64]. The PDF was calculated by a Fourier transformation of S(q) with a q_{max} = 25 Å^{-1}:

$$G(r) = \frac{2}{\pi} \int_{q_{min}}^{q_{max}} q(S(q) - 1) \sin(qr) dq \qquad (1)$$

TABLE IV: Summary of the Rietveld refinements depicted in Fig.5. Goodness of the fits are R_{wp}=0.046, R_p=0.035,χ^2=55.62 for the sample Au-4; and R_{wp}=0.054, R_p=0.044, χ^2=1913 for the sample Au-3.

sample	Au-4			Au-3		
	Au	Fe_3O_4	FeO	Au	Fe_3O_4	FeO
scale	0.982	0.359	5.149	0.116	0.531	1.360
a,b,c (Å)	4.0847(3)	8.4774(68)	4.2824(16)	4.0504(5)	8.3913(51)	4.2327(15)
$U_{iso}(Au)(Å^2)$	0.0295(3)	-	-	0.0126(5)	-	-
$U_{iso}(O)(Å^2)$	-	0.8000(370)	0.0148(49)	-	0.7948(315)	0.0031(24)
$U_{iso}(Fe_a)(Å^2)$	-	0.0254(33)	0.0502(32)	-	0.0331(32)	0.0021(10)
$U_{iso}(Fe_b)(Å^2)$	-	0.0474(38)	-	-	0.0500(72)	-

The PDF for both samples are plotted in Fig.5(b,d). We used the averaged structures obtained from the Rietveld refinements as a starting point in the PDF data analysis. The scale factor, lattice constant, ADPs and linear atomic correlation factor δ_1 were refined for each phase in the range of 1-50 Å. The model with three cubic phases of Au, FeO and Fe_3O_4 provides a good description of the data with the discrepancy of Rw=0.14 and Rw=0.11 for samples Au-3 and Au-4, respectively (Tab.V). The convergence of G(r) function at higher r due to the finite-size of our particles and limited q-resolution[34,65] prevented us from refining dimensions of Fe_3O_4 nanoparticles, which were fixed to the values obtained with SANS/SAXS experiments.

The lattice parameters derived from PDF refinement are in good agreement with those reported from Rietveld analysis. The results indicate a substantial difference between lattice constants of all three phases for Au-3 and Au-4 samples. The lattice constant of Au (4.09 Å) in Au-4 is close to the value of bulk Au (4.08 Å), while it is smaller (4.05 Å) in sample Au-3 (Fig.6a). We conclude that the reduction in size of Au nanoparticle leads to reduction of its lattice constant, consistent with the previous reports[66]. It is not the case for Fe_3O_4 nanoparticles. Despite they are of similar size in both samples, the lattice constant of magnetite in the sample Au-4 is larger than in the sample Au-3 (Fig.6b). The same tendency persists for the FeO phase (Fig.6c). Overall, there is a clear correlation of the iron oxides lattice constants with the lattice constant of the Au seed nanoparticles (Fig.6d).

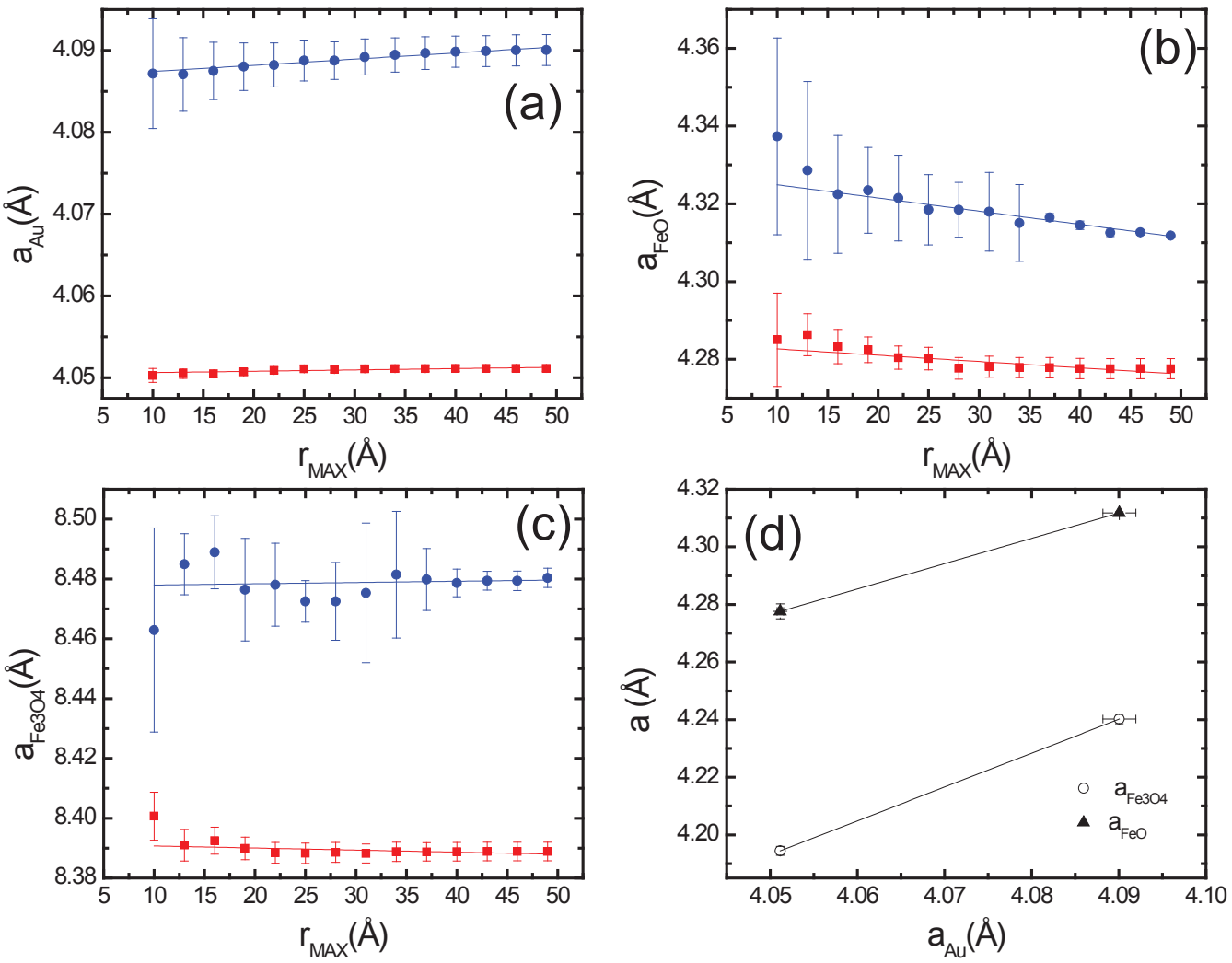

FIG. 6: Lattice constants of (a) Au, (b)FeO and (c) Fe_3O_4 nanoparticles obtained from PDF refinement as a function of r_{max} for Au-4 (•) and Au-3 (■) samples. (d) The lattice constant of Fe_3O_4(◯) and FeO (▲) as a function of Au lattice constant for both samples. Solid lines are linear fits to the data.

Our PDF model assumes a mixture of three spheres with no interface or epitaxial linkage between them. It means that possible bonds at the Au/FeO and Fe_3O_4/FeO interfaces are not included into the model. It explains the non-random difference curve, particularly at low r (see insets in Fig.5(b,d)) and suggests that not every inter-atomic distances are taken into account by our model. However, the model is good enough to clearly discriminate various phases of iron oxide and provide a reliable crystallographic information about dumbbell nanoparticles on a local scale.

TABLE V: Summary of the x-ray PDF refinements results for Au-3 Au-4 samples for r=1-50 Å. The instrument resolution Qdamp and Qbraod, as well as q_{max} = 23 Å^{-1} were fixed during the refinements.

Au-3				Au-4		
phase	Au	Fe_3O_4	FeO	Au	Fe_3O_4	FeO
scale factor	1.11(2)	0.39(2)	0.21(2)	1.42(14)	0.22(15)	0.12(8)
a,b,c (Å)	4.052(1)	8.389(3)	4.278(3)	4.090(2)	8.481(3)	4.312(1)
δ_1	1.54(7)	1.81(12)	1.82(14)	1.72(21)	1.08(21)	2.94(75)
R (nm)	3.6(2)	8.4	0	5.4 (1.4)	8.4	0
$U_{11,22,33}(Au)$(Å^2)	0.009(2)	-	-	0.0117(14)	-	-
$U_{11,22,33}(O)$(Å^2)	-	0.0143(23)	0.048(7)	-	0.0163(63)	0.0354(75)
$U_{11,22,33}(Fe_a)$(Å^2)	-	0.0084(13)	0.017(2)	-	0.0106(27)	0.0212(23)
$U_{11,22,33}(Fe_b)$(Å^2)	-	0.0165(18)	-	-	0.0352(65)	-
R_w	0.14			0.11		

IV. DISCUSSION

Previous magnetization measurements of Au-Fe_3O_4 dumbbell and flower-like nanoparticles suggested the altered magnetic state of Fe_3O_4 nanoparticles as an origin of the exchange bias effect[9,10,24,27]. The ferrimagnetic state of bulk Fe_3O_4 is a result of two competing interactions: (i) AFM interactions via super-exchange between Fe ions in the tetrahedral(A) and octahedral(B) sites and (ii) FM interactions via double-exchange between Fe ions in the octahedral sites. The exchange integrals for the bulk magnetite are J_{AB}=-22 K and J_{BB}=3 K[21]. They depend on $\cos^2\phi$, where ϕ is the cation-anion-cation angle, as well as on the cation-anion distance. The quantitative dependence of integrals on angle and distance is unclear, but in general smaller cation-anion distances and angles close to 180^o lead to the largest values of J. The magnetic state of Fe_3O_4 nanoparticles is very different compared to its bulk counterpart. Finite-size effects result in a smaller coordination number of surface atoms which weakens exchange interactions. Missing cations or anions imbalance the number of antiferromagnetic and ferromagnetic sublattices, leading to a distorted arrangement of the surface spins. The variation of ϕ angle due to internal tensile strain can further affect

the strength of the exchange interactions[67]. Combination of these effects lead to the magnetic state of Fe_3O_4 nanoparticles best described by the ferrimagnetically ordered core and canted-spins shell[15].

In principle, coupling between ordered core and disordered shell can lead to the exchange bias effect[68]. However, previous reports found no evidence of the exchange bias in the single component Fe_3O_4 nanoparticles with size larger than 6 nm, in agreement with our results[14,19,68]. This lack of exchange coupling between core and shell is likely due to a small number of the surface spins. The exchange bias effect was predicted for 1.25 nm Fe_3O_4 nanoparticles, in which 55% of all atoms reside at the surface[69,70]. For 9.8 nm Fe_3O_4 nanoparticles used in our work, this number is dramatically decreased down to 10%. However, in the dumbbell nanoparticles the number of the canted spins can be increased at the interface with Au nanoparticles. Canted spins which are characterized by possibly shorter cation-anion distances and variation of ϕ angle, can be probed by analysis of the PDF data. In the PDF model with Au and Fe_3O_4 phases only, we refined positions of Fe and O atoms in the dumbbell nanoparticles. The refinement was done for the range r = 1.5-50 Å, with the step of 3 Å. Such strategy allows us to refine the smaller volumes of Fe_3O_4 nanoparticles at the time, rendering the fact that only small portion of interface atoms can be distorted. Refinements of position of Fe atoms in both tetrahedral and octahedral sites show no apparent r-dependence and remain a constant within experimental error. We found the angle between A-B Fe ions ϕ_{AB}=124.5(3)^o, in the excellent agreement with the value of 125^o reported for the bulk magnetite[21,71]. The refined Fe-O and Fe-Fe distances Au-3 sample were 2.08(1) and 2.98(1) Å. Both of them are in excellent agreement with the values determined from PDF refinements of bulk Fe_3O_4: 2.07 and 2.97 Å[71]. Of course, it is worth nothing that refinements of the PDF data with only two phases of Au and Fe_3O_4, resulted in rather poor quality of fits, with Rw =0.35 and 0.42 for the samples Au-3 and Au-4, respectively. Only introduction of the third FeO phase improved the fits and reduced Rw down to 0.14 and 0.11. Nevertheless, we tried to refine Fe and O positions in the three-phase model, but only marginal improvement of the fit was observed. It is fair to say that the crystal structure of Fe_3O_4 nanoparticles in the dumbbell samples remains similar to its bulk counterpart, at least within the accuracy of our model.

The antiphase boundaries (APBs) were responsible for the EB effect observed in thin films of Fe_3O_4 deposited on MgO substrate[72]. The lattice constants of Fe_3O_4 are almost double

of those for MgO and Au. Thus, heteroepitaxy is possible in both cases and formation of APBs can be expected in Fe_3O_4 nanoparticles in the dumbbell samples. The APBs are stacking faults naturally occurring during island growth mode in heteroepitaxy. Because of the difference in lattice constant and symmetry, the different Fe_3O_4 islands can be shifted or rotated during the growth[72]. Across APBs the AFM interactions (J_{AA}) between A sublattice Fe ions are greatly increased[21]. Consequently, they can be exchange coupled to the neighboring ferromagnetic regions, where FM interactions (J_{BB}) are dominant. The APBs can be directly observed with high-resolution transmission electron microscopy (HRTEM) or scanning transmission electron microscope (STEM), as the regions of irregular shape with a darker contrast (see for example, HRTEM images of Fe_3O_4 thin films in[73]). Fig.8 shows the STEM images of a single Fe_3O_4 nanoparticle in the Au-3 sample. Lines of atoms extend in perfect registry from the core to the surface and no signs of APBs are evident (Fig.8b). The stacking faults associated with APBs can be modeled in the analysis of the PDF data. For example, in CdSe nanoparticles density faults as large as 50% were observed as unphysically large values of anisotropic atomic displacement parameters U_{33} for Se atoms in the PDF model[74]. We found no improvements of the fit with introducing anisotropic atomic displacement parameters (U_{11}=U_{22}≠U_{33}) for both O and Fe atoms. However, U_{ii} values obtained for Fe atoms in the dumbbell nanoparticles are twice larger (see Tab.V) compared to the values obtained for the bulk. Based on STEM studies and analysis of the PDF data, we must conclude that the APBs are absent in our dumbbell nanoparticles and cannot account for the EB effect. Overall, we can reject the altered magnetic state of Fe_3O_4 nanoparticles as the origin of the exchange bias effect in the dumbbell nanoparticles.

Magnetite can be oxidized into hematite (α-Fe_2O_3). Hematite crystallizes in the rhombohedral structure and become AFM below 260 K[26]. In principle, co-existing of the AFM hematite and FiM magnetite phases in the dumbbell nanoparticles can explain the EB effect. However, the rhombohedral structure of hematite can be unambiguously distinguished from the cubic structure of magnetite with x-ray diffraction experiments. Moreover, our reference bulk sample consisted of 80% of Fe_3O_4 and 20% of α-Fe_2O_3, which was measured in the identical experiential conditions as the dumbbell nanoparticles. Two phases were clearly detectable and provided an excellent reference. Rietveld and PDF refinements found no evidence of the hematite phase in the dumbbell nanoparticles. It is not surprising, considering that our dumbbell nanoparticles have not been exposed to the temperatures as

high as 550 ^{o}C, which are required for oxidation of Fe_3O_4 into α-Fe_2O_3[75]. We also tried to introduce maghemite phase (γ-Fe_2O_3) into the PDF refinements. Maghemite has a very similar crystal structure to magnetite and co-existing of the two phases have been previously reported in iron oxide nanoparticles[76]. However, the best quality of the fit obtained with dual γ-Fe_2O_3/Fe_3O_4 phases was Rw=0.32, while the model with FeO/Fe_3O_4 phases resulted in a much better fit with Rw=0.14 (for the sample Au-3).

The x-ray diffraction and magnetization measurements suggest the presence of antiferromagnetic FeO phase in the dumbbell nanoparticles. Hence, we conclude that the exchange bias effect observed in the dumbbell nanoparticles is the result of the coupling between antiferromagnetic FeO and ferrimagnetic Fe_3O_4 phases, consistent with the previous reports on FeO/Fe_3O_4 composite nanostructures[35,62,63,77,79–81]. The question is what is the origin of the FeO phase in our dumbbell nanoparticles? The nanostructures with FeO and Fe_3O_4 phases can be obtained either by oxidation of FeO nanoparticles or by reduction of Fe_3O_4 nanoparticles. Sun *et al*, oxidized the surface of FeO nanoparticles by introducing dry air into the solution of FeO nanoparticles at 25, 60 and 100 ^{o} C to synthesize FeO-core/Fe_3O_4-shell nanoparticles[35]. Similarly, the FeO nanoparticle solution was washed out several times and exposed to air for 5-120 days, resulting in formation of the FeO-core/Fe_3O_4-shell structures[62,63,79,81]. The synthesis of FeO/Fe_3O_4 nanoparticles consists of two steps: synthesis of FeO nanoparticles and their further oxidation in air. The synthesis of FeO is achieved by decomposing $Fe(CO)_5$ in a solvent mixture that had a weak oxidizing agent "pyridine N-oxide" that partially oxidizes the Fe to FeO[79]. In our samples, the $Fe(CO)_5$ was decomposed under an Ar atmosphere and the oxidizing agent was absent. Thus, the formation of FeO nanoparticles in the dumbbell nanoparticles prior to oxidation is unlikely. Finally, we used the same synthesis to obtain free Fe_3O_4 nanoparticles, where no evidence of the FeO phase was found. If single component Fe_3O_4 nanoparticles were formed after oxidation was completed, another plausible explanation of coexisting of FeO and Fe_3O_4 phases is a partial reduction of magnetite. The Fe_3O_4-core/FeO-shell nanoparticles were synthesized at 550^{o}C in the ultra-high vacuum by partially reducing the surface of Fe_3O_4 nanoparticles into FeO[83]. Obviously, this scenario can be excluded in our samples, because they have not been exposed to such high temperature and vacuum. In what follows we suggest that the partial reduction of Fe_3O_4 into FeO occurs at the interface with Au nanoparticles.

Because of the catalytic applications of Au nanoparticles, their electronic structure has

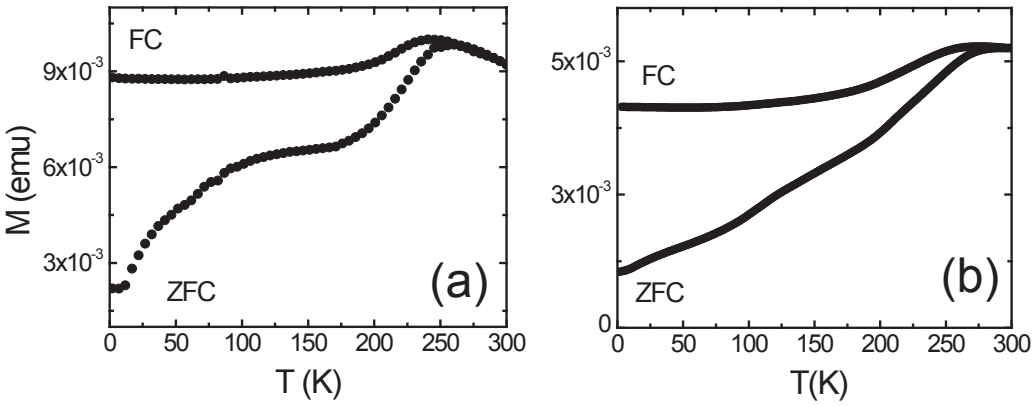

FIG. 7: Comparison of ZFC and FC M(T) magnetizations for (a) fresh Au-3 sample and (b) the same sample aged for 23 months.

been intensively studied[18,27,28,84]. The charge transfer from Au nanoparticles to the adjacent metal in bimetallic nanostructures or to the capping agent, dramatically modifies the electron configuration of Au on the nanoscale. The famous example is the ferromagnetism observed in small Au nanoparticles coated with the thiol-group surfactant. The strong charge transfer from Au surface atoms to S resulted in generation of holes in 5d orbitals. Those holes were able to sustain ferromagnetic moments even at room temperature[18]. Similarly, the ferromagnetic behavior was observed in $Au_{48}Pt_{52}$ nanowires, due to d-charge transfer from Au to the Pt site[85]. The Au nanoparticles were also found to change the electronic properties of the oxide substrates. For instance, Au nanoparticles deposited on a TiO_2 substrate showed very high catalytic activity, because Au nanoparticles partially reduces TiO_2 at the interface. This interface is believed to be the most active part of the catalyst[84]. The charge transfer from Au to Fe_3O_4 was observed in Au-Fe_3O_4 nanostructures, including dumbbells, with x-ray absorption techniques[27,28]. The charge transfer resulted in increase of Fe^{2+} valence state in magnetite and formation of Au-O and Au-Fe bonds, presumably across Au/Fe_3O_4 interface[27]. In the magnetite, for every four O^{2-} anions there are two Fe^{3+} and one Fe^{2+} cations. If the charge balance is violated by the increased number of Fe^{2+} cations, the reduction of magnetite can occur to lower electrostatic energy: $Fe_3O_4 \rightarrow$ 3FeO +O. As a result, FeO phase and excess of oxygen are formed. The reduction of magnetite nanoparticles takes place at the Au/Fe_3O_4 interface. The limited diffusion path of 5d electrons transferred from Au, confines formation of FeO phase to the vicinity of the interface region, thus the Fe_3O_4/FeO structure is sustained. STEM measurements of Au-3 sample

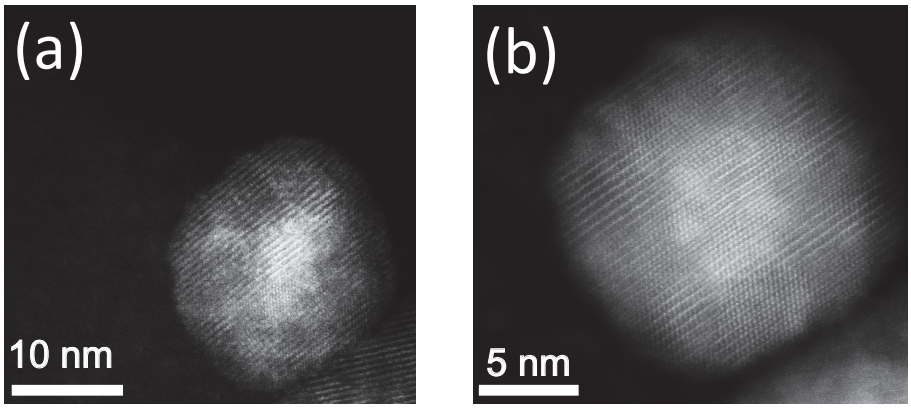

FIG. 8: (a)The STEM image of a Fe_3O_4 nanoparticle in the sample Au-3. (b) The same image at higher magnification.

provide limited support for this conclusion, showing the contrast variation across a single magnetite nanoparticle (Fig.8a). The interior of this nanoparticle appears to be brighter than exterior, suggesting Fe_3O_4-rich core and FeO shell structure[81].

The reduction of Fe_3O_4 at the interface with Au nanoparticles will lead to the excess of oxygen atoms. We suggest that those oxygen atoms formed Au-O bonds at the interface between gold and magnetite. Formation of Au-O bonds in the dumbbell nanoparticles was previously observed with XPS measurements[27]. The formation of the Au-O bonds can also explain imperfection of our PDF model. The model used for refinement of the x-ray PDF could not reproduce the first peak at r$\sim$ 2.01 Å for both samples (see insets in Fig.5b,d). The position of this peak does not correspond to the C-C bond length of 1.540 Å, reported for the oleic-acid coated Fe_3O_4 nanoparticles[76]. The best fit of the peak consists of two separate Gaussian peaks with very different widths: broad G_1, which is responsible for the majority of the intensity in this r-range, and G_2, which is less intense with the peak position shifted towards larger distances (Fig.9). The position of G_2 peak in the sample Au-4 corresponds to the nearest-neighbor Fe-Fe distance of $\sim$ 2.15 Å in the magnetite. The width of this peak is consistent with the ADP parameter for this phase at 300 K. The position of G_1 peak, however cannot be indexed with any interatomic distances in all three phases present in our model. The width of G_1 is a factor of two larger than of G_2 for both samples. If the G_1 peak were to belong to a crystallographic model one would expect it to be narrower as compare to the G_2 peak, due to highly correlated inter-atomic motions which sharpen the

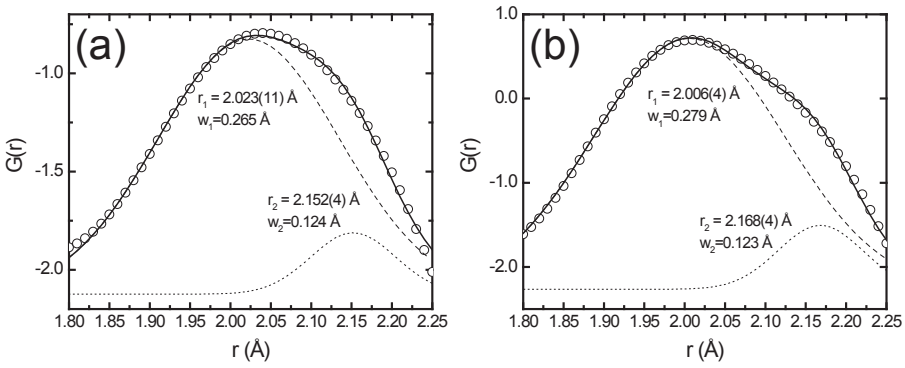

FIG. 9: Fits of the low r region of x-ray PDF for samples (a) Au-4 and (b) Au-3. Dashed line is the broad and dotted line is the narrow Gaussian. Solid line is the sum of both.

peaks at lower r. It is certainly not the case. Position of the G_1 peak is equal to 2.023(11) and 2.006(4) Å for Au-4 and Au-3 samples, respectively. Both comparable with 2.03(7) Å value reported for the Au-O bonds in Fe_3O_4-Au nanostructures[27]. Although the location of Au-O bonds cannot be determined from PDF measurements, we hypothesize that they are formed at the Au/Fe_3O_4 interface as a result of the partial reduction of the magnetite phase.

Fig.6a shows that lattice constant of Au nanoparticles is considerably reduced in smaller nanoparticles (sample Au-3) compared to the larger ones (Au-4). It is in agreement with previous reports, which suggested that the lattice size of a metal nanoparticle shrinks with decrease of a particle size[86]. In contrary, the lattice size of small metal oxide nanoparticles expands, presumably due to modifications of the attractive potential[87–89]. The lattice constant of Fe_3O_4 nanoparticles are very different in the sample Au-3 and Au-4, despite they are of the same size in each sample. The lattice constant a=8.481 Å of Fe_3O_4 nanoparticles in the sample Au-4 is larger than the value of 8.395 Å in the bulk magnetite. In the sample Au-3 the lattice constant a=8.389 Å is *smaller* than the bulk value. Apparently, finite-size effects have no obvious impact on the lattice dimensions of Fe_3O_4 nanoparticles in the dumbbell samples. We think that such significant difference in lattice size of Fe_3O_4 nanoparticles is due to their epitaxial linkage to the seed Au nanoparticles. In thin films the deposited layer adopts the crystalline structure of a substrate during epitaxy. The same effect was observed in the FeO nanoparticles deposited Au and Pt substrates. The lattice of FeO nanoparticles was found to be larger when deposited on Au(111) substrate than on Pt(111) substrate, because the lattice constant of Au is larger than the one of Pt. Our

findings suggest that this is the case for the dumbbell nanoparticles as well. The lattice constants of both FeO and Fe_3O_4 are correlated with the lattice constant of the seed gold nanoparticles; however more data points are needed to quantify this correlation (Fig.6d). The reduction of Fe_3O_4 to FeO presumably occurs across the Au/Fe_3O_4 interface, which is larger in sample Au-4, thus it may explain the enhancement of H_{EB} observed in this sample. More spins at the interface are exchange coupled and higher magnetic fields are required to reverse the magnetization of the FiM layer[80]. The bulk wüstite FeO is unstable and can undergo spontaneously phase transformation into the spinel-like structure of maghemite or magnetite after 10 days.[81]. Therefore, the effect of the interfacial area on H_{EB} can be directly probed by magnetization measurements of the aged dumbbell sample. Fig.7 compares M(T) measurements of the freshly synthesized Au-3 sample, and the same sample aged for 23 months. There is no clear peak in the ZFC magnetization at T_N=190 K of FeO phase for the aged sample. The FC magnetization loop shows the negative shift in the horizontal direction, with smaller H_{EB}=980 Oe as compared with H_{EB}=1350 Oe of as-synthesized Au-3 sample (Fig.3). We hypothesize that the reduction of H_{EB} is related to FeO volume change. For example, decreasing of FeO volume resulted in reduction of H_{EB} in thin film systems[80]. Interestingly, FeO phase can be still detected in nanoparticles even after 23 months, indicating that in contrast to the bulk FeO, only part of FeO transforms into Fe_3O_4, consistent with the previous reports[23,78]. The partial reduction presumably occurs due to diffusion of Fe^{2+} and Fe^{3+} ions in oxygen sublattice and charge transfer between Fe ions of different valence[79].

The exchange bias effect in composite nanoparticles is far more complex than in thin films, even of the same composition[90]. For example, Co-core/CoO-shell nanoparticles show non-monotonic dependence of H_{EB} on the size of the Co core, in contrast to thin films where $H_{EB} \sim 1/t_{FM}$, where t_{FM} is the thickness of FM layer[80]. The nonmonotonic dependence can be understood by appealing to neutron diffraction measurements carried out on Co/CoO nanoparticles, which demonstrated a relation between H_{EB} and strain induced by the lattice mismatch between Co and CoO shell[91]. Strikingly, Fig.10 shows the dependence of H_{EB} on the lattice mismatch between FeO and Fe_3O_4 for both dumbbell samples at various temperature, where larger H_{EB} are observed in the sample Au-4 with a smaller lattice mismatch. We hypothesize that this lattice mismatch can be responsible for the strain-induced magnetic moment at the Fe_3O_4/FeO interface, not unlike in Co/CoO nanoparticles[12]. Presumably,

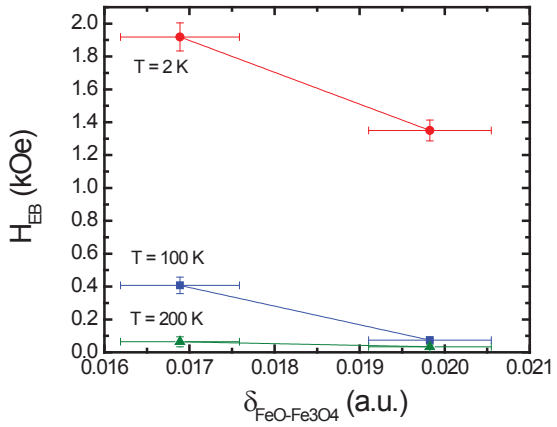

FIG. 10: The exchange bias field H_{EB} as a function of lattice mismatch δ between FeO and Fe_3O_4 at 2K (•), 100K (■) and 200 K (▼).

the interface magnetic moment is lower in sample Au-4 with the bulk-like Au seed nanoparticles. It is however, increased in the sample Au-3, where smaller lattice constant of Au nanoparticles lead to more canted interface between FeO and Fe_3O_4. The magnitude and relation of this interface magnetic moment with the volume of FeO phase are yet to be studied with neutron diffraction experiments. If this relation is demonstrated, it opens new ways to control H_{EB} in the dumbbell nanoparticles by simply changing dimensions of Au seed nanoparticles, which is a simpler way to achieve higher H_{EB} as compared to synthesizing flower-like structures with poorly controlled magnetic state[11].

V. CONCLUSIONS

Using combination of magnetization, SANS, SAXS, x-ray PDF and STEM measurements we elucidated the origin of the EB effect in the Au- Fe_3O_4 dumbbell nanoparticles, with similar size of Fe_3O_4 nanoparticles (9.8 nm) and different sizes of the seed Au nanoparticles 4.1 and 2.7 nm, for samples Au-4 and Au-3, respectively. Both dumbbell samples show similar T_B= 285 K and clear AFM-type transition at 190 K, corresponding to the Néel temperature of FeO. The Rietveld and PDF analysis of the synchrotron x-ray diffraction data confirmed the presence of FeO phase in both dumbbell nanoparticles, which is unstable and diminishing over time. The origin of the FeO phase is due the charge transfer from

Au to Fe_3O_4, which increases the number of Fe^{+2} ions in magnetite. This leads to the formation of FeO via reduction of the Fe_3O_4 phase. The excess of the oxygen during the reduction forms Au-O bonds, as evident from the analysis of PDF data at lower r. The independent confirmation of Fe_3O_4/FeO interface was obtained with STEM, which showed Fe_3O_4-rich core/FeO-shell structure of the magnetite nanoparticles in the sample Au-3. The EB effect was observed for both samples at temperatures below T_B. H_{EB} was found to be the largest in the sample Au-4, with larger size of Au seed nanoparticles. The EB effect was not observed in the reference sample consisting of the mixture of single component Au and Fe_3O_4 nanoparticles, as well as no AFM transition at around 190 K was found. The finite-size effects result in reduced lattice constant of the Au nanoparticles in the Au-3 sample, while the lattice constant found in the sample Au-4 is similar to the bulk value of Au. The lattice constant of Fe_3O_4 nanoparticles is reduced in the sample Au-3 as compared with the sample Au-4, despite the same size of Fe_3O_4 nanoparticles in both samples. The lattice contraction of FeO phase was observed as well in the sample Au-3. The epitaxial linkage between Fe_3O_4 and Au nanoparticles leads to the reduction of the lattice constant of Fe_3O_4, which adopts the smaller lattice volume of Au nanoparticles in the Au-3 sample. The large surface area between Fe_3O_4 and FeO phases in the sample Au-4 leads to a higher H_{EB}, as compared with the sample Au-3. We found an evidence that H_{EB} depends on the lattice mismatch between Fe_3O_4 and FeO phases, however more neutron scattering experiments are needed to understand this dependence. The additional TEM Electron Energy Loss Spectroscopy (EELS) measurements of the dumbbell nanoparticles are being pursued to identify the location and oxidation state of FeO phase and provide independent conformation for the presence of Au-O bonds. The method has been successfully used in the past to determine oxidation states of transition metal oxide systems on nanoscale[92,93].

VI. ACKNOWLEDGEMENT

We are grateful to W. Dmowski and Y. Tong for helping with the x-ray measurements. We thank J. Simonson for his help with magnetization measurements at BNL. We also acknowledge P. Konarev, S. Disch, J. C. Neuefeind and K. Page for the stimulating discussions. V.S.U. acknowledges support by the Materials Sciences and Engineering Division, Office of Basic Energy Sciences, U.S. Department of Energy. Portions of this research at Oak Ridge

National Laboratorys High Flux Isotope Reactor and Brookhaven National Laboratory's National Synchrotron Light Source were sponsored by the Scientific User Facilities Division, Office of Basic Energy Sciences, U.S. Department of Energy. The Office of Biological and Environmental Research of the U.S. Department of Energy sponsored neutron data collection on the CG-3 Bio-SANS instrument. The part of this research was conducted at the Center for Nanophase Materials Sciences (ORNL) and Center for Functional Nanomaterials (BNL), which are sponsored by the Scientific User Facilities Division, Office of Basic Energy Sciences, U.S. Department of Energy. This research used resources of the Advanced Photon Source, a U.S. Department of Energy (DOE) Office of Science User Facility operated for the DOE Office of Science by Argonne National Laboratory under Contract No. DE-AC02-06CH11357. Work at Brookhaven National Laboratory (CM and MCA) was carried out under the auspices of the US Department of Energy, Office of Basic Energy Sciences, Contract DE-AC02-98CH1886.

---

* Electronic address: feygensonm@ornl.gov

[1] K. C.-F. Leung, S. Xuan, X. Zhu, D. Wang, C.-P. Chak, S.-F. Lee, W. K.-W. Ho, B. C.-T. Chung, Chem. Soc. Rev., **41**, 1911 (2012).

[2] S. M. Janib, A. S. Moses and J. A. Kackay, Adv. Drug Delivery Rev., **62**, 1052 (2010).

[3] C. Sun, J. S. H. Lee and M. Zhang, Adv. Drug Delivery Rev., **60**, 1252 (2008).

[4] T. Hasan, P. Rai, S. Mallidi, X. Zheng, R. Rahmanzadeh, Y. Mir, S. Elrington and A. Khurshid, Adv. Drug Delivery Rev., **62**, 1094 (2010).

[5] C. Xu, B. Wang and S. Sun, J. Am. Chem. Soc., **131**, 4216 (2009).

[6] C. S. Thaxton, D. G. Georganopoulou and C. A. Mirkin, Clin. Chim. Acta, **363**, 120 (2006).

[7] A. S. K. Hashmi and G. J. Hutchings, Angew. Chem., Int. Ed.,**45**, 7896 (2006).

[8] A. Arcadi, Chem. Rev., **108**, 3266 (2008).

[9] S. Chandra, N. A. F Huls, M. H Phan, S. Srinath, M. A. Garcia, Y. Lee, C. Wang, S. Sun, O. Iglesias, H. Srikanth, Nanotechnology **25**, 055702 (2014).

[10] N. A. Frey, S. Srinath, H. Srikanth, C. Wang, and S. Sun, IEEE Transactions on Magnetics **45**, 3094 (2007).

[11] N. A. Frey, M. H. Phan, H. Srikanth, S. Srinath, C. Wang, and S. Sun, J. Appl. Phys. **105**,

07B502 (2009).

[12] M. Feygenson, Y. Yiu, A. Kou, K. S. Kim, and M. C. Aronson, Phys. Rev. B **81**, 195445 (2010).

[13] M. Feygenson, A. Kou, L. E. Kreno, A. L. Tiano, J. M. Patete, F. Zhang, M.- S. Kim, V. Solovyov, S. S. Wong, M. C. Aronson, Phys. Rev. B **81**, 014420 (2010).

[14] G. F. Goya, T. S. Berquo, F. C. Fonseca and M. P. Morales, J. Appl. Phys. **94**, 3520 (2003).

[15] K. L. Krycka, R. A. Booth, C. R. Hogg, Y. Ijiri, J. A. Borchers, W. C. Chen, S. M. Watson, M. Laver, T. R. Gentile, L. R. Dedon, S. Harris, J. J. Rhyne, S. A. Majetich, Phys. Rev. Lett. **104**, 207203 (2010).

[16] A. G. Roca, M. P. Morales, K. O'Grady and C. J. Serna, Nanotechnology **17**, 2783 (2006).

[17] K. Page, Th. Proffen, H. Terrones, M. Terrones, L. Lee, Y. Yang, S. Stemmer, R. Seshadri, and A. K. Cheetham, Chem. Phys. Lett. **393**, 385 (2004).

[18] P. Crespo, R. Litrán, T. C. Rojas, M. Multigner, J. M. de la Fuente, J. C. Sánchez-López, M. A. García, A. Hernando, S. Penadés, A. Fernández, Phys. Rev. Lett. **93**, 087204 (2004).

[19] R. K. Zheng, G. H. Wen, K. K. Fung, and X. X. Zhang, J. Appl. Phys. **95**, 5244 (2004).

[20] R. H. Kodama, A. E. Berkowitz, E. J. McNiff, S. Foner, Phys. Rev. Lett. **77**, 394 (1996).

[21] D. T. Margulies, F. T. Parker, M. L. Rudee, F. E. Spada, J. N. Chapman, P. R. Aitchison, and A. E. Berkowitz, Phys. Rev. Lett. **79**, 5162 (1997).

[22] D. T. Margulies, F. T. Parker, F. E. Spada, R. S. Goldman, J. Li, R. Sinclair, A. E. Berkowitz, Phys. Rev. B **53**, 9175 (1996).

[23] F. Pineider, C. Fernandez, V. Videtta, E. Carlino, A. al Hourani, F. Wilhelm, A. Rogalev, P. D. Cozzoli, P. Ghigna, C. Sangregorio, ACS Nano **7**, 857 (2013).

[24] E. Umut, F. Pineider, P. Arosio, C. Sangregorio, M. Corti, F. Tabak, A. Lascialfari, P. Ghigna, J. Magn. and Magn. Mater. **324**, 2373 (2012).

[25] J. Nogués, V. Skumryev, J. Sort, S. Stoyanov, and D. Givord, Phys. Rev. Lett., **97**, 157203 (2006).

[26] M. J. Benitez, D. Mishra, P. Szary, G. A. Badini Confalonieri, M. Feyen, A. H. Lu, L. Agudo, G. Eggeler, O. Petracic, H. Zabel, J. Phys.: Condens. Matter **23**, 126003 (2011).

[27] F. Lin and R. Doong, J. Colloid Interf. Sci., **417**, 325 (2014).

[28] M. Kim, H. Song, J. Mater. Chem. C, **2**, 4997.

[29] Y. F. Han, J. H. Wang, D. Kumar, Z. Yan, D. W. Goodman, J. Catal., **232**, 467 (2005).

[30] S. Peng, Y. Lee, C. Wang, H. Yin, S. Dai, S. Sun, Nano. Res. **1**, 229 (2008).

[31] H. Yu, M. Chen, P. M. Rice, S. X. Wang, R. L. White, S. Sun, Nano Lett. **5**, 379 (2005).

[32] W. T. Heller, V. S. Urban, G. W. Lynn, K. L. Weiss, H. M. O'Neill, S. V. Pingali, S. Qian, K. C. Littrell, Y. B. Melnichenko, M. V. Buchanan, D. L. Selby, G. D. Wignall, P. D. Butler, D. A. Myles, J. Appl. Cryst. **47**, 1238 (2014).

[33] S. R. Kline, J. Appl. Cryst. **39**, 895 (2006).

[34] C. L. Farrow, P. Juhas, J. Liu, D. Bryndin, E. S. Bozin, J. Bloch, Th. Proffen and S. J. L. Billinge, J. Phys: Condens. Mat.,**19**, 335219 (2007).

[35] X. Sun, N. F. Huls, A. Sigdel and S.Sun, Nano. Lett., **12**, 246 (2012).

[36] H. Khurshid, S. Chandra, W. Li, M. H. Phan, G. C. Hadjipanayis, P. Mukherjee and H. Srikanth, J. Appl. Phys. **113**, 17B508 (2013).

[37] E. Lima Jr., A. L. Brandl, A. D. Arelaro, and G. F. Goya, J. App. Phys. **99**, 083908 (2006).

[38] P. Tartaj, C. J. Serna, Chem. Mater. **14**, 4396 (2002).

[39] S.K. Sharma, J.M. Vargab, K.R. Pirota, S. Kumar, C.G. Lee and M. Knobel,J. Alloys and Compounds **509**, 6414 (2011).

[40] E. P. Wohlfarth, J. Magn. Magn. Mater., **39**, 39 (1983).

[41] M. F. Hansen, S. Morup, J. Magn. Magn. Mater., **184**, 262 (1998).

[42] C. Petit, A. Taleb, M.-P. Pileni, Adv. Mater., **10**, 259 (1998).

[43] R. P. Borges, W. Guichard, J. G. Lunney, J. M. D. Coey, and F. Ott, J. Appl. Phys. **89**, 3868 (2001).

[44] K. Oguz, P. Jivrajka, M. Venkatesan, G. Feng, and J. M. D. Coey, J. Appl.Phys. **103**, 07B526 (2008).

[45] E. J. W. Verwey, Nature (London) **144**, 327 (1939).

[46] R. Prozorov, T. Prozorov, S. K. Mallapragada, B. Narasimhan, T. J. Williams, D. A. Bazylinski, Phys. Rev. B **76**, 054406 (2007).

[47] A. Mitra, J. Mohapatra, S. S. Meena, C. V. Tomy, M. Aslam J. Phys. Chem. C **118**, 19356 (2014).

[48] P. K. Manna, S. M. Yusuf, Phys. Rep. **61**, 535 (2014).

[49] I. V. Golosovsky, G. Salazar-Alvarez, A. Lopez-Ortega, M. A. Gonzalez, J. Sort, M. Estrader, S. Surinach, M. D. Baro, J. Nogues, Phys. Rev. Lett. **102**, 247201 (2009).

[50] P. Bartlett, and R. H. Ottewill, J. Chem. Phys. **96**, 3306 (1992).

[51] J. Teixeira, J. Appl. Cryst., **21**, 781 (1988).

[52] H. Kaya, J. Appl. Cryst., **37**, 223 (2004).

[53] H. Kaya and N-R deSouza, J. Appl. Cryst., **37**, 508 (2004).

[54] A. Guenther, J.-P. Bick, P. Szary, D. Honecker, C. D. Dewhurst, U. Keiderling, A. V. Feoktystov, A. Tschoepe, R. Birringer, A. Michels, J. Appl. Cryst., **47**, 992 (2014).

[55] A. Wiedenmann, J. Appl. Cryst. **33**, 428 (2000).

[56] A. Wiedenmann, A. Hoell, M. Kammel and P. Boesecke, Phys. Rev. E **68**, 031203 (2003).

[57] M. Klokkenburg, B. H. Erne, A. Wiedenmann, A. V. Petukhov, and A. P. Philipse, Phys. Rev. E **75**, 051408 (2007).

[58] L.W. Finger, D.E. Cox and A. P. Jephcoat, J. Appl. Cryst. **27**, 892 (1994).

[59] J. Nanda, S. Sapra, D. D. Sarma, N. Chandrasekharan, and G. Hodes, Chem. Mater. **12**, 1018 (2000).

[60] Z. Kaszkur, Z. Kristallogr. **23**, 147 (2006).

[61] Y. Hou, Z. Xu, and S. Sun, Angew. Chem. Int. Ed., **46**, 6329 (2007).

[62] S.K. Sharma, J.M. Vargas, K.R. Pirota, Shalendra Kumar, C.G. Lee, and M. Knobel, J. Alloys Compd.**509**, 6414 (2011).

[63] D. W. Kavich, J. H. Dickerson, S. V. Mahajan, S. A. Hasan, and J.-H. Park, Phys. Rev. B **78**, 174414 (2008).

[64] X. Qiu, J.W. Thompson, and S. J. L. Billinge, J. Appl. Crystallogr. **678**, 37 (2004).

[65] K. Kodama, S. Iikubo, T. Taguchi, and S. Shamoto, Acta Crystallogr., Sect. A: Found. Crystallogr. **62**, 444 (2006).

[66] K. Page, Th. Proffen, M. Niederberger, and R. Seshadri, Chem. Mater. **22**, 4386 (2010).

[67] K. Balakrishnan, S. K. Arora, I. V. Shvets, J. Phys.: Condens. Matter **16**, 5387 (2004).

[68] J. Nogués, C. Leighton, and I. K. Schuller, Phys. Rev. B **61**, 1315 (2000).

[69] J. Mazo-Zuluaga, J. Restrepo, F. Muñoz, and J. Mejîa-López, J. Appl. Phys. **105**, 123907 (2009).

[70] J. Mazo-Zuluaga, J. Restrepo, J. Mejîa-López, J. Phys: Condens. Mat.,**20**, 195213 (2008).

[71] F. de Boer, J. H. van Santen, E. J. W. Verwey, J. Chem. Phys. **18**, 1032 (1950).

[72] S. K. Arora, R. G. S. Sofin, A. Nolan, I. V. Shvets, J. Magn. and Magn. Mater. **286**, 463 (2005).

[73] W. Eerenstein, T. T. M. Palstra, T. Hibma, and S. Celotto, Phys. Rev. B **68**, 014428 (2003).

[74] A. S. Masadeh, E. S. Bozin, C. L. Farrow, G. Paglia, P. Juhas, S. J. L. Billinge, A. Karkamkar, and M. G. Kanatzidis, Phys. Rev. B **76**, 115413 (2007).

[75] K. J. Gallagher, W. Feitknecht and U. Mannweiler, Nature **217**, 1118 (1968).

[76] S. Disch,'The spin strcuture of magnetic nanoparticles and in magnetic nanostrcutures', PhD thesis, University of Aachen (2011).

[77] Z. Swiatkowska-Warkocka, K. Kawaguchi, H. Wang, Y. Katou, and N. Koshizaki, Nanoscale Research Letters **6**, 226 (2011).

[78] M. Estrader, A. Lopez-Ortega, I. V. Golosovsky, S. Estrade, A. G. Roca, G. Salazar-Alvarez, L. Lopez-Conesa, D. Tobia, E. Winkler, J. D. Ardisson, W. A. A. Macedo, A. Morphis, M. Vasilakaki, K. N. Trohidou, A. Gukasov, I. Mirebeau, O. L. Makarova, R. D. Zysler, F. Peiro, M. Dolors Baro, L. Bergstroem, J. Nogues, Nanoscale **7**, 3002 (2015).

[79] F. X. Redl, C. T. Black, G. C. Papaefthymiou, R. L. Sandstrom, M. Yin, H. Zeng, C. B. Murray, S. P. OBrien, J. Am. Chem. Soc., **126**, 14583 (2004).

[80] J. Nogués and I. Schuller, J. Magn. and Magn. Mater. **192**, 203 (1999).

[81] C.-J. Chen, R.-K. Chiang, H.-Yi Lai and C.-R. Lin, J. Phys. Chem. C **114**, 4258 (2010).

[82] A. Lak, M. Kraken, F. Ludwig, A. Kornowski, D. Eberbeck, S. Sievers, F. J. Litterst, H. Weller, M. Schilling, Nanoscale **5**, 12286 (2013).

[83] D. Wilson, M. A. Langell, Appl. Surf. Sci., **303**, 6 (2014).

[84] D. Matthey, J. G. Wang, S. Wendt, J. Matthiesen, R. Schaub, E. Lgsgaard, B. Hammer, F. Besenbacher, Science **315**, 1692 (2007).

[85] X. Teng, M. Feygenson, Q. Wang, J. He, W. Du, A. I. Frenkel, W. Han, M. Aronson, Nano Lett., **9**, 3177 (2009).

[86] C.W. Mays, J. S. Vermaak, D. Kuhlmann-Wilsdorf, Surf. Sci. **12**, 134 (1968).

[87] K. Ishikawa and T. Uemori, Phys. Rev. B **60**, 11841 (1999).

[88] G. Li, J. Boerio-Goates, B. F. Woodfield, and L. Li, Appl. Phys. Lett. **85**, 2059 (2004).

[89] V. Perebeinos, S. W. Zhang, and F. Zhang, Solid State Commun. **123**, 295 (2002).

[90] J. Nogués, J. Sort, V. Langlais, V. Skumryev, S. Suriñach, J. S. Muñoz, and M. D. Baró, Physics Reports **422**, 65 (2005).

[91] S. E. Inderhees, J. A. Borchers, K. S. Green, M. S. Kim, K. Sun, G. L. Strycker, and M. C. Aronson, Phys. Rev. Lett. **101**, 117202 (2008).

[92] S. Estrade, Ll. Yedra, A. Lopez-Ortega, M. Estrader, G. Salazar-Alvarez, M.D. Baro, J. Nogues, F. Peiro, Micron **43**, 30 (2012).

[93] Ll. Yedra, E. Xuriguera, M. Estrader, A. Lopez-Ortega, M. D. Baro, J. Nogues, M. Roldan, M.

Varela, S. Estrade, F. Peiro, Microsc. Microanal., **20**, 698 (2014).